Bioactive Materials 20 (2023) 539–547

Contents lists available at ScienceDirect

Bioactive Materials

journal homepage: www.keaipublishing.com/en/journals/bioactive-materials

Increasing stiffness promotes pulmonary retention of ligand-directed dexamethasone-loaded nanoparticle for enhanced acute lung inflammation therapy

Yinglan Yu, Shujie Li, Yuan Yao, Xinran Shen, Lian Li, Yuan Huang *

Key Laboratory of Drug-Targeting and Drug Delivery System of the Education Ministry and Sichuan Province, Sichuan Engineering Laboratory for Plant-Sourced Drug and Sichuan Research Center for Drug Precision Industrial Technology, West China School of Pharmacy, Sichuan University, Chengdu, 610041, China

ARTICLE INFO

Keywords:
Pulmonary drug delivery
Mucus barrier
Epithelial barrier
Stiffness
Ligand modification
Acute lung inflammation

ABSTRACT

Inhaled nanoparticles (NPs) need to penetrate the bronchial mucosa to deliver drug payloads deeply in the lung for amplified local therapy. However, the bronchial mucociliary barrier eliminates NPs rapidly, which considerably limits their mucosal penetration. In this study, we find that surface ligand modification and stiffness adjustment of NPs contribute to the significantly enhanced bronchial mucosal absorption and pulmonary retention of inhaled drugs. We utilize neonatal Fc receptor ligand (FcBP) to modify the rationally designed low stiffness NPs (Soft-NP) and high stiffness NPs (Stiff-NP) to target bronchial mucosa. In an acute lung inflammation rat model, after intranasal administration with dexamethasone-loaded NPs, Stiff-NP endowed with FcBP displays superior therapeutic effects. The *in vitro* data demonstrate that the promotion effect of FcBP to bronchial mucosal absorption of Stiff-NP dominates over Soft-NP. This could be attributed to the higher affinity between ligand-receptor when incorporating FcBP on the Stiff-NP surface. Meanwhile, high stiffness modulates more actin filaments aggregation to mediate endocytosis, along with strengthened Ca^{2+} signal to enhance exocytosis. Conclusively, we highlight that FcBP-modified NPs with higher stiffness would be a potential pulmonary drug delivery system.

1. Introduction

Pulmonary drug delivery is a promising approach for the local treatment of lung diseases [1–3]. Unfortunately, drawbacks such as rapid clearance and short residence time of inhaled drugs severely restrict their efficient therapeutics [4]. The lung mainly consists of the trachea, bronchi, alveolar ducts, and alveolar sacs [5]. Prolonged lung retention of drugs requires deposition in the bronchial tree after inhalation and penetrating the bronchial epithelium into deep lung tissue [6]. However, drugs are readily eliminated by the mucus and ciliated epithelial barriers upon reaching the bronchus [5,7]. Therefore, an ideal pulmonary drug delivery system requires to not only achieve bronchial deposition but also rapidly cross the bronchial mucosa.

Nanocarriers have received mounting attention in pulmonary drug delivery, as they could improve drug stability and protect cargo from pH/enzyme damage on the mucosal surface [8–10]. Several studies indicated that the physicochemical properties of nanoparticles (NPs) would impact their pulmonary retention [11–13]. As reported, particle size is a vital factor in determining the pulmonary deposition site of inhaled NPs, and the size of NPs smaller than 200 nm are prone to deposit in the bronchi [14–16]. Also, the ligand modification strategies have been reported to increase the pulmonary retention effect of NPs during recent years, which employed integrins, folate, transferrin, etc., as targeting ligand [17–19]. However, there are still some other issues that should be considered, for example, the effect of stiffness of NPs on the pulmonary drug delivery, the interaction between stiffness and ligand modification on the bronchial epithelium permeability and pulmonary retention.

Herein, we fabricated low stiffness NPs (Soft-NP) and high stiffness NPs (Stiff-NP), respectively. Soft-NP and Stiff-NP with surface decorated with neonatal Fc receptor ligand (FcBP) to target bronchial mucosa were fabricated as Soft-NP-F and Stiff-NP-F. Then, the contributions of stiffness and ligand were investigated. The *in vivo* therapeutic evaluation on acute lung inflammation rat model showed that the anti-inflammatory

Peer review under responsibility of KeAi Communications Co., Ltd.
* Corresponding author.
E-mail address: huangyuan0@163.com (Y. Huang).

https://doi.org/10.1016/j.bioactmat.2022.06.016
Received 15 February 2022; Received in revised form 20 June 2022; Accepted 22 June 2022

effect of intranasally administrated dexamethasone (Dex)-loaded NPs enhanced as the stiffness increased. FcBP modification strikingly promoted the bronchial mucosal absorption of NPs, and enabled superior transcytosis of Stiff-NP over Soft-NP. Further mechanism studies revealed that such improvements were related to actin filaments-mediated endocytosis and Ca^{2+} signals-conducted exocytosis. Taken together, this work advanced our understanding of the roles of stiffness and ligand modification on NPs in pulmonary drug delivery and provided insight that FcBP-modified NPs with high stiffness would be a promising vehicle for delivering therapeutic agents into the lung.

2. Results and discussion

2.1. Higher stiffness and FcBP modification improves acute lung inflammation/injury therapy

In this study, we developed lipid NPs with different stiffness by packaging poly (lactic-co-glycolic acid) (PLGA) NPs into the hollow lipid bilayers (Fig. 1A). Hollow liposomes were prepared by the film dispersion method and referred to as Soft-NP. PLGA cores were fabricated using the self-emulsifying solvent evaporation method (Fig. S1). Then bare PLGA cores were encapsulated in liposomes to obtain Stiff-NP. The water layer of the lipid NPs decreased with the increased size of the PLGA cores (Fig. S2) thus leading to higher stiffness of NPs [20–22]. Besides, Soft-NP and Stiff-NP showed homogeneously spherical shapes (Fig. S3).

The mechanical properties of NPs were validated using a quartz crystal microbalance (QCM). Changes in resonant frequency and deposition mass indicated the saturation of NPs over 1.5 h exposure (Fig. 1B–C, deep lines, and Fig. S4). The dissipation factor of Soft-NP (Fig. 1B, light lines) was higher than that of Stiff-NP (Fig. 1C, light lines), demonstrating the lower stiffness. Modeling of resonant frequency and dissipation factor data were used to determine the shear modulus of Soft-NP and Stiff-NP as 84.51 ± 5.83 KPa and 2020.47 ± 39.22 KPa, respectively (Fig. 1D), indicating variable stiffness of NPs as the amount of water layer changes.

NPs were further modified with FcBP to target neonatal Fc receptor (FcRn) which was overexpressed in the bronchial epithelium [23,24]. The FcBP-modified Soft-NP and Stiff-NP were defined as Soft-NP-F and Stiff-NP-F, respectively. Soft-NP-F and Stiff-NP-F had similar FcBP

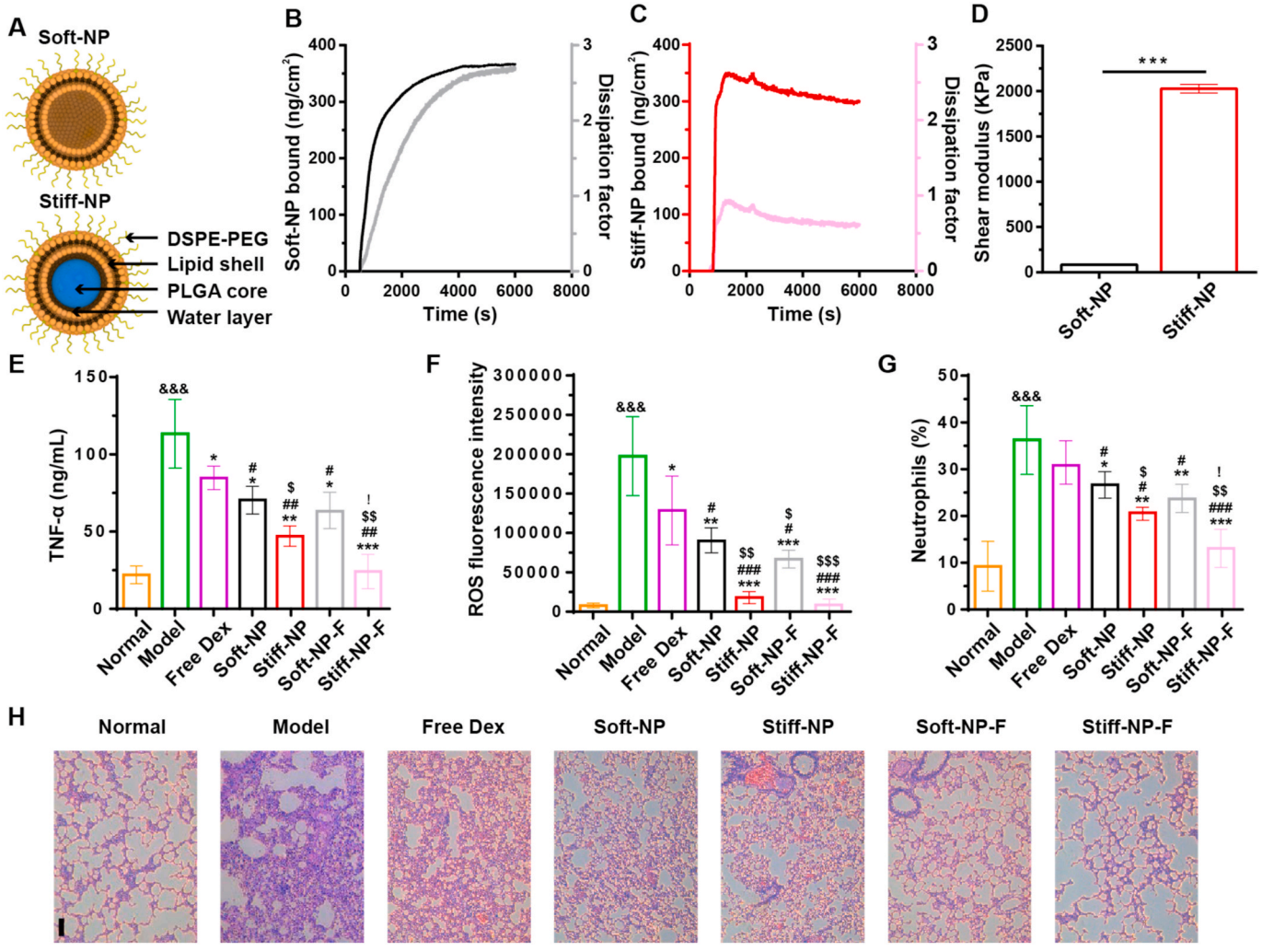

Fig. 1. Fabrication and *in vivo* anti-inflammatory effects of nanoparticles (NPs). (A) Graphical representation of the NPs fabrication. The stiffness increased as less interfacial water exist. QCM analysis of Soft-NP (B) and Stiff-NP (C). The real-time monitoring for deposition of NPs to the sensor's surface was detected by QCM. Dissipation factor (light lines) increased concurrently with the accumulation of NPs mass (deep lines) on QCM surfaces. (D) QCM modeling determined the shear modulus of NPs. ***$p < 0.001$. Mean ± SD, n = 3. (E) TNF-α in BALF were measured using ELISA. (F) The ROS levels in pulmonary tissues from rats with LPS-induced ALI and subjected to different treatments. (G) Quantitative analysis of neutrophils in pulmonary tissues of ALI rats. (H) Hematoxylin-eosin (H&E) stained pathological sections of lung tissues. Scale bar: 100 μm *$p < 0.05$, **$p < 0.01$, ***$p < 0.001$ versus model group; #$p < 0.05$, ##$p < 0.01$, ###$p < 0.001$ versus free Dex; $ $p < 0.05$, $$ $p < 0.01$, $$$ $p < 0.001$ versus Soft-NP; &&& $p < 0.001$ versus normal; ! $p < 0.05$ versus Stiff-NP. Mean ± SD, n = 6.

modification rates (Table S1). FcBP-modified NPs also showed homogeneously spherical shapes (Fig. S5). All FcBP-modified NPs (FcBP NP) and unmodified NPs (PEG NP) exhibited similar sizes of 100–150 nm with negative surface charges (Fig. S6). The colloidal stability results showed that all NPs remained stable in rat bronchoalveolar lavage fluid (BALF) for 12 h with negligible size variations (Fig. S7).

To investigate the influence of stiffness and FcBP modification on the therapeutic efficacy of acute lung inflammation/injury (ALI), we intranasally dosed lipopolysaccharide (LPS)-challenged rats with free dexamethasone (Dex) or Dex-loaded NPs. We prepared Dex-loaded NPs with similar diameters and drug loading (Table S2). The FcBP modification and Dex loading did not significantly influence Young's modulus of NPs (Fig. S8). All Dex-loaded NPs showed relatively sustained drug release (Fig. S9). The anti-inflammatory study *in vitro* showed that Stiff-NP-F significantly reduced the pro-inflammatory cytokine TNF-α level (Fig. S10). In the present study, administration of LPS resulted in a significant increase in the lung wet/dry weight ratio (Fig. S11), TNF-α (Fig. 1E), reactive oxygen species (ROS) level (Fig. 1F), and neutrophils (Fig. 1G), indicating the successful establishment of LPS induced ALI model. In this study, free Dex failed to significantly reduce neutrophils, which was consistent with previous literature and could be attributed to the rapid mucociliary clearance/blood absorption of inhaled corticosteroids, thereby resulting in poor lung pharmacokinetics and short action duration of Dex [25,26]. In contrast, treatment with Dex-loaded NPs significantly relived the pulmonary inflammation, and the anti-inflammatory effect was further enhanced as the NPs stiffness increased. Interestingly, FcBP modification significantly improved the therapy of both NPs, and the therapeutic outcome of Stiff-NP-F to treat ALI was better than Soft-NP-F. These phenomena were also demonstrated by the histological analysis of lung tissues (Fig. 1H). The lung injury score and infiltrating cell count significantly increased in the model group compared to normal rat (Table S3). All these pathologic perturbations were significantly alleviated in the Stiff-NP-F group.

Lung vascular permeability is another pathological hallmark of ALI [27]. As shown in Fig. S12, the total cell counts and protein content in BALF of the model group significantly increased, indicating successful modeling. After treatment with Dex-loaded NPs, the total cell counts and protein content all decreased. In particular, protein content decreased to an approximate normal level after treatment with Stiff-NP-F. Evans blue was further used to assess vascular wall permeability as it can quantitatively bind to plasma albumin (Fig. S13A) [28–30]. As shown in Fig. S13B, among all the groups, the lungs of the model group showed the deepest and widest blue, which was significantly alleviated after Dex-loaded NPs treatment. Quantitative analysis of Evans blue extravasation in the lungs samples further confirmed the high lung vascular permeability of the model rat, and the Evans blue amount decreased in the Dex-loaded NPs groups as NPs became stiffer and modified with FcBP (Fig. S13C). Stiff-NP-F treatment resulted in the lowest Evans blue

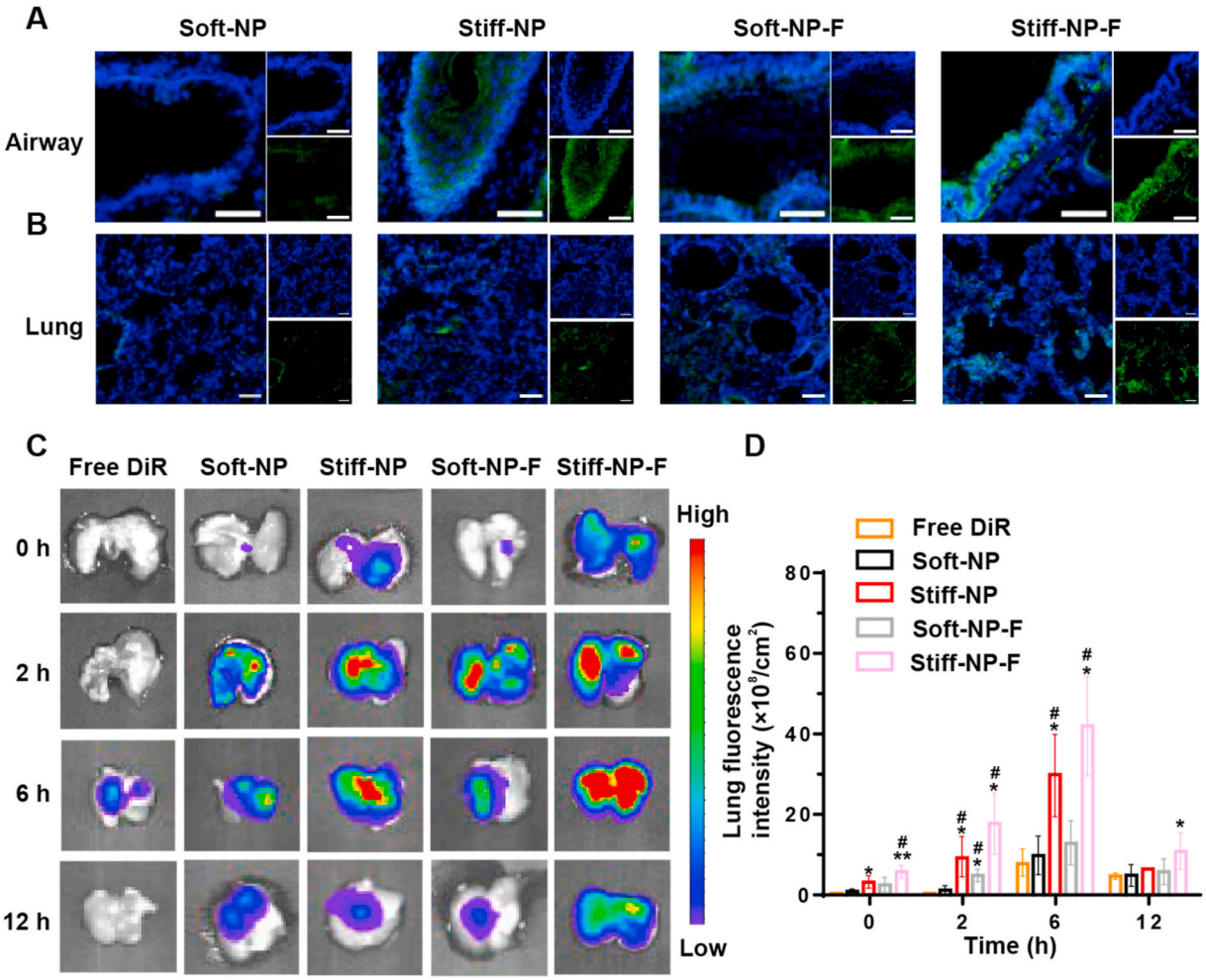

Fig. 2. The distribution and retention of NPs in the lungs. (A) Representative images of the *in vivo* distribution of coumarin 6 (C6)-labeled NPs (green) in the airways of rats. The cell nucleus was stained with DAPI (blue). Scale bars: 20 μm. (B) Rats lungs distribution of NPs (green) at 30 min after administration. The cell nucleus was stained with DAPI (blue). Scale bars: 50 μm. (C) Representative images for NPs exposed lungs over time. (D) Quantitative determination of NPs in the mice lungs. *$p < 0.05$, **$p < 0.01$ versus free DiR, #$p < 0.05$ versus Soft-NP. Data represent mean ± SD (n = 3).

leakage, demonstrating the outstanding protective effects of Dex-loaded NPs against high vascular permeability induced by LPS.

Collectively, we prepared lipid NPs with different stiffness and our results revealed two important features of stiffness and ligand in NPs-mediated ALI therapy: (1) without FcBP modification, the anti-inflammatory effect of NPs enhanced as the stiffness increased; (2) upon FcBP modification, the therapeutic efficacy of both NPs significantly improved, but the performance of Stiff-NP-F was significantly superior over that of Soft-NP-F.

2.2. *Higher stiffness and FcBP modification enhances the lungs distribution and retention*

Then the biodistribution of NPs in the airways and lungs was investigated upon intranasal administration. As shown in Fig. 2A–B, strong fluorescence of Stiff-NP in both rats' bronchus and lungs were observed, whereas such distribution of Soft-NP was limited. Semi-quantification of fluorescence further demonstrated that Stiff-NP had higher accumulation in bronchus and lungs than Soft-NP (Fig. S14). Surprisingly, FcBP modification significantly improved the distribution of both NPs, maybe because of the over-expression of FcRn in the airways and lungs (Fig. S15). Thus, Stiff-NP-F exhibited the highest distribution in the bronchus and lungs among all NPs. In addition, higher fluorescence of C6-loaded Stiff-NP-F was observed in the rat inflamed lung, indicating enhanced lung accumulation (Fig. S16). Besides, Stiff-NP-F had higher endocytosis in neutrophils than other NPs.

Next, the retention of NPs in the lungs was measured at predetermined time points. The results of *ex vivo* imaging showed that the mice pulmonary accumulation of DiR-loaded NPs was higher than that of free DiR (Fig. 2C and Fig. S17). Consistent with confocal imaging results (Fig. 2B), Stiff-NP demonstrated significantly enhanced lung accumulation ($p < 0.05$) compared to Soft-NP at 6 h post-administration (Fig. 2D). Notably, FcBP modification improved the accumulation of both NPs in the lungs. Importantly, Stiff-NP-F had significantly higher

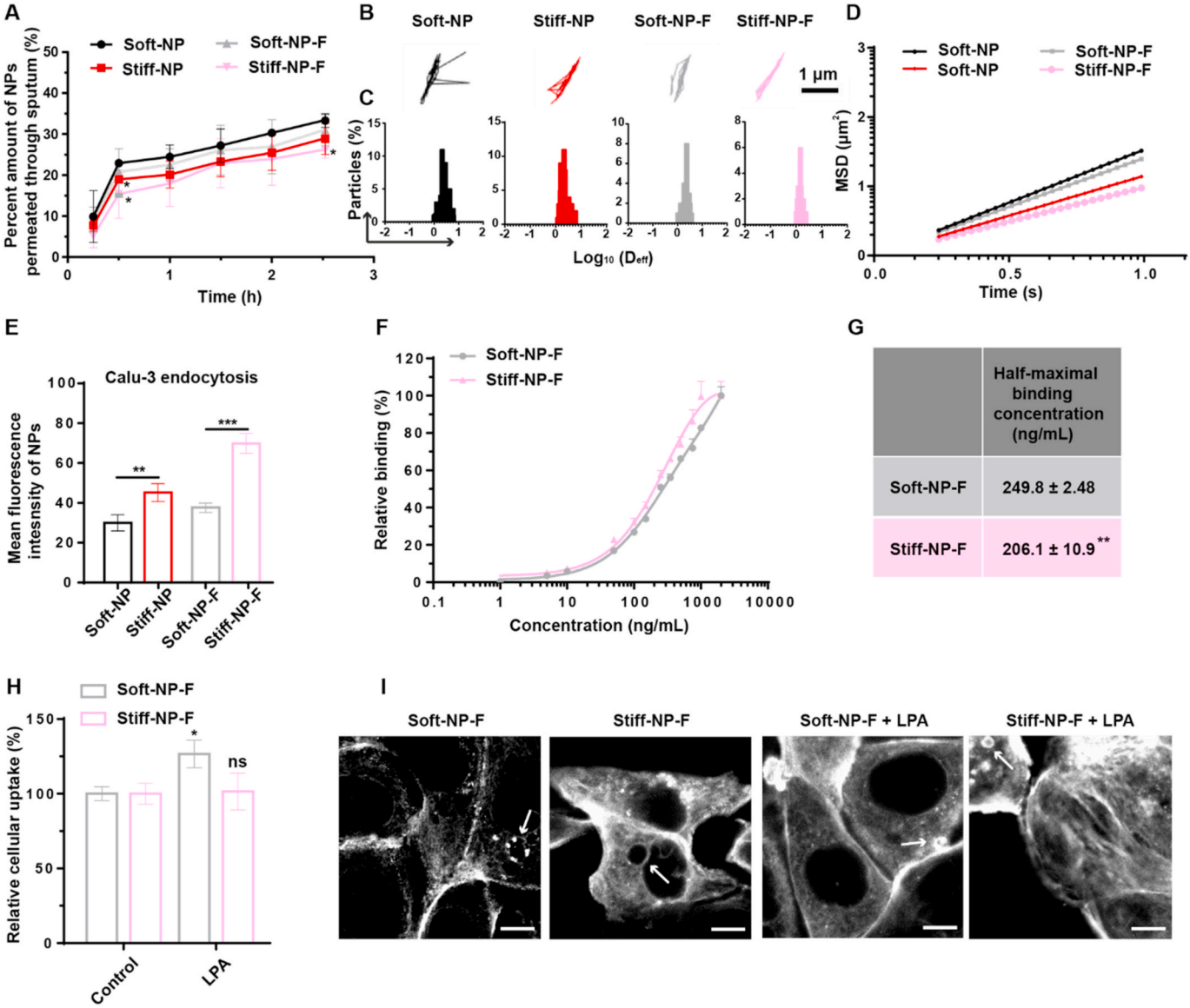

Fig. 3. Sputum penetration and endocytosis of NPs. (A) Percent amount of C6-loaded fluorescent NPs permeated through human sputum in transwells. *$p < 0.05$, versus Soft-NP. Mean ± SD, n = 3. (B) Representative trajectories of NPs at a time scale of 1 s. (C) Distributions of the logarithms of diffusion coefficient (D_{eff}) for NPs at a time of 1 s. (D) Ensemble-averaged geometric mean square displacement (MSD) in human sputum by nanoparticle tracking analysis (NTA). (E) The cellular uptake of NPs. **$p < 0.01$, ***$p < 0.001$. Mean ± SD, n = 3. (F) Concentration-dependent binding curves of NPs. (G) Half-maximal binding concentrations. **$p < 0.01$ versus Soft-NP-F. Mean ± SD (n = 3). (H) Stimulation of uptake of soft NPs by LPA. *$p < 0.05$, ns $p > 0.05$ versus control. (I) Organization of actin filaments following the feeding of NPs, with or without the additional incubation with LPA. Arrow was the actin cup. Scale bar: 10 μm.

pulmonary accumulation than the other groups ($p < 0.05$) at 12 h post-administration, indicating its prolonged residence time. Overall, these results showed that FcBP-modified NPs with higher stiffness could enhance pulmonary accumulation by utilizing the advantageous combination of high stiffness and FcBP ligand: (1) higher stiff NPs were more prone to accumulate in the lung; (2) FcBP modification could facilitate a higher lung distribution of both NPs; (3) stiffness modulation and ligand modification jointly improved pulmonary accumulation and prolonged residence time.

2.3. Stiffness modulation and FcBP modification profoundly affect the endocytosis process

Following the lungs distribution, in-depth studies on the process of bronchial epithelial transporting were conducted. The mucus penetration, the first step for bronchial epithelial absorption, was investigated. As shown in Fig. 3A, Soft-NP exhibited higher sputum penetration efficiency than Stiff-NP, and FcBP modification did not significantly change the penetration behavior of NPs, indicating that the stiffness would affect the mucus penetrating capacity of NPs in cystic fibrosis (CF) sputum. This could be further demonstrated by the results of particle trajectories (Fig. 3B), diffusion coefficient (D_{eff}, Fig. 3C), and the median mean-squared displacement (MSD, Fig. 3D).

We next investigated the endocytosis of NPs on human bronchial epithelial Calu-3 cells, which expressed FcRn (Fig. S18). As shown in Fig. 3E and Fig. S19, the endocytosis of Stiff-NP was significantly higher than Soft-NP; after FcBP modification, the endocytosis of Stiff-NP-F experienced a considerable enhancement, while that of Soft-NP-F increased slightly. These results raised a fundamental question: which step in NPs endocytosis was coordinated by stiffness and ligand.

The endocytosis of NPs through epithelial cells initially starts with the binding of NPs to cell membranes *via* ligand-receptor recognition, followed by internalization [31]. Thus the cellular binding was investigated by incubating Calu-3 cells with the FcBP decorated NPs at 4 °C. Fig. 3F–G showed that the Stiff-NP-F had higher binding avidity than Soft-NP-F.

Then, the mechanism of the endocytic pathway was explored. As shown in Fig. S20, clathrin-mediated endocytosis inhibitor chlorpromazine significantly reduced the cellular uptake of Soft-NP, Stiff-NP, and Soft-NP-F, but not Stiff-NP-F, indicating the endocytosis of Stiff-NP-F was barely mediated by clathrin [32]. Moreover, the addition of lovastatin and amiloride showed that the uptake of all the NPs was related to caveolae-mediated endocytosis and micropinocytosis [33–35].

The actin cytoskeleton has been demonstrated to involve in the FcRn-mediated internalization as well as the response of NPs in macrophages to mechanical properties of NPs [36]. Thus, lysophosphatidic acid (LPA), an activator of several signaling pathways, was adopted to stimulate the actin filaments [37]. As shown in Fig. 3H, LPA incubation greatly stimulated the internalization of Soft-NP-F. However, Stiff-NP-F and PEG NP treatment upon LPA stimulation showed no changes in endocytosis (Fig. 3H and Fig. S21A). Actin polymerization has been recognized as the main force for the cells to push the leading membrane edge and engulf NPs [38]. Initially, an actin cup that is comprised of a dense actin network forms beneath the NPs. As additional actin filaments remodeling occurs, the actin cup transforms into an actin ring around the NPs, resulting in the endocytosis of both membrane and NPs [39–41]. To further explore the mechanism of this phenomenon, rhodamine-phalloidin was used to stain the actin filaments. As shown in Fig. 3I and Figs. S21B–C, after incubation with Soft-NP-F, cells formed actin filaments but failed to exhibit an intact actin cup or ring. Notably, actin filaments became more concentrated with observable actin cups upon Stiff-NP-F treatment. Interestingly, the formation of an actin cup is a clear indicator of the initiation of endocytosis, which was observed in Soft-NP-F after stimulation with LPA. A possible explanation for this might be that the endocytosis of Stiff-NP-F was sufficient to stimulate the actin reorganization for better internalization, while Soft-NP-F was unable to activate enough actin filaments which were required for the FcRn-mediated uptake.

Collectively, Stiff-NP-F was beneficial for FcRn-mediated endocytosis for the following reasons: (1) Stiff-NP-F was more conducive to the binding of NPs onto cell membranes; (2) Stiff-NP-F could stimulate the actin filaments reorganization for greater internalization of NPs.

2.4. Stiffness and FcBP modification synergistically promote exocytosis

The exocytosis of bronchial mucosal epithelial cells to deep lung tissue, which is a vital step for enhancing drugs' pulmonary residence, was further studied. As shown in Fig. 4A, without FcBP modification, Stiff-NP exhibited higher exocytosis than their soft counterpart; after FcBP modification, the exocytosis of FcBP NP was significantly enhanced and Stiff-NP-F showed higher exocytosis than Soft-NP-F.

In the secretion pathway of NPs, after being transported by the endoplasmic reticulum (ER) and Golgi complex, NPs get released to the extracellular matrix. The confocal laser scanning microscope (CLSM) images and the Pearson correlation coefficients (Rr) displayed that both the colocalization with ER and Golgi of PEG NP increased as their stiffness raised (Fig. 4B–C and Fig. S22). Similarly, the colocalization with ER-Golgi of the FcBP NP also enhanced with their stiffness improved. Besides, Stiff-NP-F was more prone to be transported in ER secretion pathway compared with Soft-NP-F.

To understand the underlying mechanism, we further explored whether NPs stiffness has an effect on the intracellular calcium (Ca^{2+}), as Ca^{2+} is reported to participate in FcRn-mediated phagocytosis and ER is one of the important calcium storages [42,43]. After incubating with NPs, Ca^{2+} signals elevated in the form of transient rises or spikes (Fig. 4D and Fig. S23). As the NPs stiffness increased, the number of Ca^{2+} signal spikes and the concentration of Ca^{2+} enhanced. Interestingly, a series of studies suggested that ER which is filled with intracellular Ca^{2+} tends to be recruited to early endosomes (EE) and fused with EE [44,45]. As shown in the CLSM images of the ER-EE fusion, higher colocalization of EE with ER was observed in Stiff-NP-F (Fig. 4E–F), which might be beneficial for NPs transporting to ER secretion pathway.

Collectively, our results confirmed the enhanced exocytosis of Stiff-NP-F, which might be explained by the fact that Stiff-NP-F could stimulate strengthed Ca^{2+} signal and induce the fusion of endosomes and ER, thereby promoting the exocytosis of Stiff-NP-F.

3. Conclusion

In summary, we have systematically investigated the effects of stiffness and ligand modification of NPs as pulmonary drug delivery carriers. Our results revealed that FcBP-modified NPs with higher stiffness exhibited extended pulmonary retention as compared with their soft counterpart. Impressively, in an acute lung inflammation rat model, after intranasal administration with dexamethasone-loaded NPs, FcBP-modified NPs with higher stiffness displayed superior therapeutic efficacy. Mechanism investigation revealed that the FcBP ligand performed better on stiff NPs owing to two aspects. First, the FcBP ligand on stiff NPs was better presented and exerted higher binding affinity towards the targeted receptors than on soft NPs. Second, the stiffness of NPs could engage stronger actin filaments aggregation and Ca^{2+} signal to enhance FcRn-mediated endocytosis and exocytosis of bronchial epithelium, respectively.

4. Materials and methods

4.1. Fabrication and characterization of nanoparticles

PLGA core was fabricated using the self-emulsifying solvent evaporation method [21]. To fabricate PLGA nanoparticles (NPs), we employed syringe pumps to introduce 1 mg PLGA acetonitrile solution (15 mg/mL) into 4 mL Pluronic F68 (F68) solution (0.25 mg/mL),

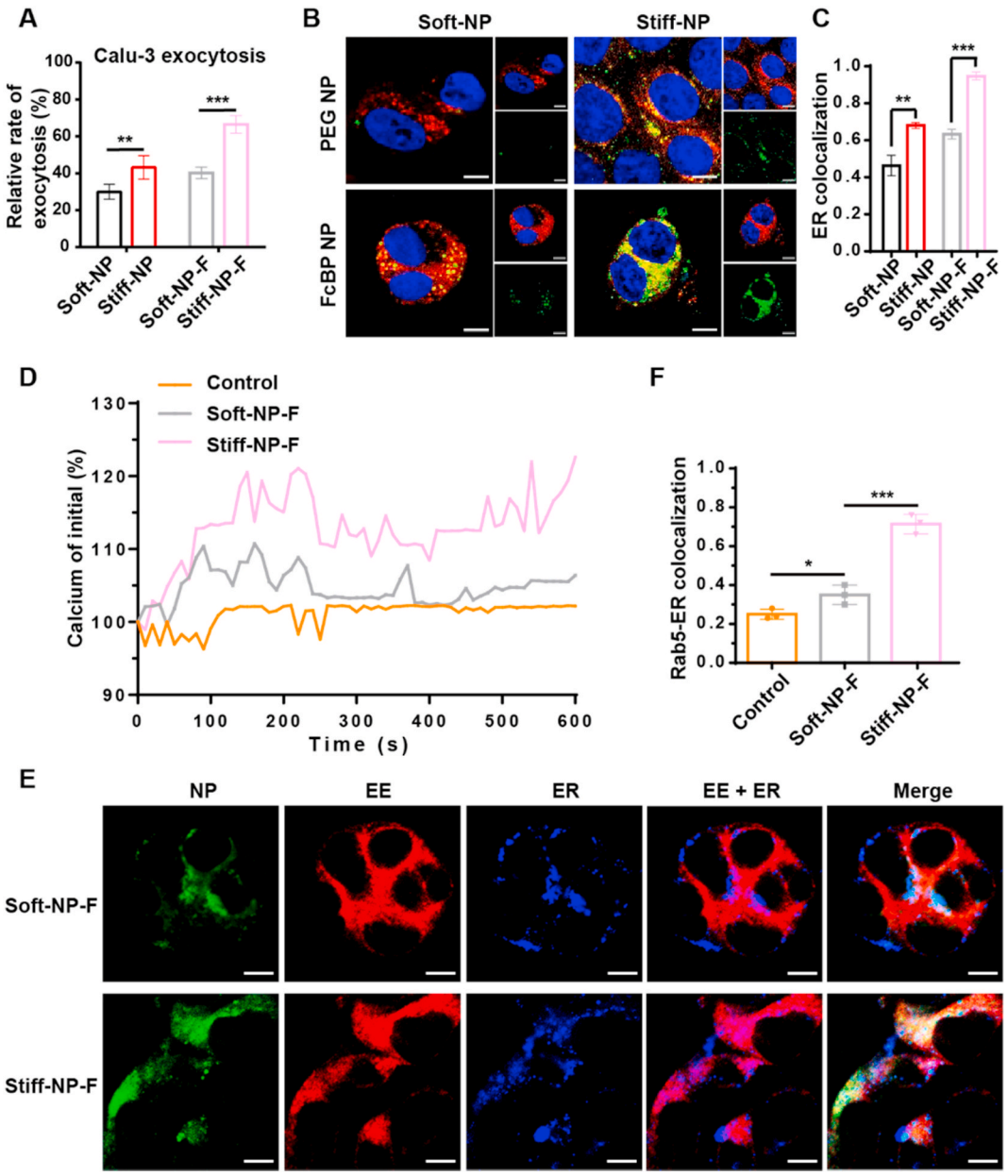

Fig. 4. The intracellular trafficking and exocytosis of NPs. (A) Exocytosis of NPs. **p < 0.01, ***p < 0.001. Mean ± SD (n = 3). The CLSM images (B) and co-localization (C) of NPs with ER. Blue: nucleus; red: ER; green: NPs. Scale bar: 10 μm **p < 0.01, ***p < 0.001. Mean ± SD (n = 3). (D) Time course of the change in Ca^{2+} in Calu-3 cells during endocytosis of FcBP-modified NPs. (E) The CLSM images of early endosomes and ER. Red: early endosomes; blue: ER; green: NPs. Scale bar: 10 μm. (F) The colocalization of early endosomes and ER. *p < 0.05, ***p < 0.001, mean ± SD (n = 3).

simultaneously drying the acetonitrile with an air pump. The PLGA cores were subsequently encapsulated into lipid NPs by an ultra-sonicator (Scientz-950E, Ningbo Scientz Biotechnology Co., Ltd, Ningbo, Zhejiang, China). Phospholipid, cholesterol, and DSPE-PEG_{2000} or DSPE-PEG_{2000}-FcBP were dissolved in 8 mL of chloroform according to the molar ratio of 40:8:1. Then chloroform was removed by a rotary evaporator (Shanghai Science and Education Equipment Co., Ltd, Shanghai, China) at 38 °C in a vacuum to form a thin film. Trace chloroform was cleared by vacuum drying overnight. The dry lipid film was then hydrated at 38 °C by adding 4 mL of distilled water or PLGA NPs solution to obtain crude lipid NPs suspensions. The crude lipid NPs solutions were finally conducted *via* an ultra-sonicator on an ice bath at 120 W for 3 min (duration 5 s with 5 s interruption) to obtain the PLGA-lipid NPs.

The NPs hydrodynamic diameters and zeta potential were studied with a Zetasizer NanoZS90 instrument (Malvern Instruments Ltd., UK). A transmission electron microscope (TEM, Tecnai G2 F20, FEI, USA) was used to examine the morphology of the PLGA-lipid NPs.

4.2. Water content studies

To characterize the presence of water inside the NPs, we used Rhodamine B (RhB) to label the water layer by applying 200 μM RhB solution (in distilled water or PLGA NPs solution) as the hydration solution. After fabrication, the free RhB were separated from NPs by a Sephadex G50 gel size-exclusion column, and the collected NPs were diluted to the same concentration. The fluorescence emission spectrum of the NPs was measured at the excitation wavelength of 510 nm by a microplate reader (SynergyH1, BioTek, Vermont, USA).

4.3. Quartz crystal microbalance

For quartz crystal microbalance (QCM) analysis, Au sensors (Biolin Scientific) were modified with amino as literature [46]. In brief, Au QCM sensors were treated in ultraviolet for 30 min and exposed to 1 mL dopamine hydrochloride (0.2 mg/mL) in Tris-based buffer (10 mM, pH = 8.5) at 20 °C for 45 min. Then the Au sensors were submerged in polyethyleneimine (PEI, 20 mg/mL) Tris-based buffer (10 mM, pH = 8.5) at 20 °C for 30 min. After that, the sensors were washed with distilled water three times, followed by drying with nitrogen. The QCM-D instrument (Q-Sense Analyzer, Biolin Scientific, Gothenburg, Sweden) was adopted for relative determination. After heating the sensors to 37 °C, baseline measurements were obtained for the dry sensors and the sensors under distilled water flowing at 20 μL/min. NPs solution (0.5 mg/mL) was introduced to the sensors after the acquisition of distilled water baseline and measurements of resonant frequency and dissipation factor were recorded over 1.5 h, followed by 0.5 h rinsing with water. Modeling of raw data to obtain deposited masses and shear modulus was completed with QTools (Biolin Scientific).

4.4. Ex vivo stability of NPs in rats bronchoalveolar lavage fluid

The *ex vivo* stability of NPs was determined according to the literature method [25]. Rats bronchoalveolar lavage fluid (BALF) was collected by lavaging the rat lungs six times with 1 mL of PBS, and the gathered fluids were merged for each animal. Subsequently, BALF samples collected from three rats were pooled, cells were separated by centrifugation (5000 rpm, 10 min), then the supernatant was collected and syringe-filtered (0.2 μm). The protein content of the BALF supernatant was determined by the BCA Protein Assay Kit (Beyotime Institute of Biotechnology, Haimen, Jiangsu, China), and diluted to 0.6 mg/mL. The NPs were added to BALF (1:9, v/v) and incubated at room temperature. At the predetermined time, the sizes of NPs were measured.

4.5. In vivo anti-inflammatory efficacy of dexamethasone-loaded NPs

The acute lung inflammation/injury (ALI) rat model was established as reported [25]. Rats were challenged twice with lipopolysaccharide (LPS, 5 mg/kg) at 0 and 6 h by intranasal instillation. After 24 h, physiological saline, free dexamethasone (Dex), or Dex-loaded NPs were administered at a dose of 1 mg/kg (n = 6). After 48 h, animals were sacrificed, BALF and lungs were collected. After centrifugation at 5000 rpm for 10 min, the BALF supernatant was collected for the enzyme-linked immunosorbent (ELISA) assay. Red blood cells in homogenized lungs were lysed with ammonium-chloride-potassium (ACK) lysing buffer. Subsequently, cells were stained with V450-conjugated anti-rat CD11b and PE-conjugated anti-rat Ly-6G for neutrophil analysis by flow cytometry. The level of reactive oxygen species (ROS) was assessed by commercial kits (Beyotime Biotech, Nantong, Jiangsu, China), and the lung histological sections were stained with hematoxylin-eosin staining (H&E).

4.6. Pulmonary accumulation study

4.6.1. Distribution of NPs in bronchi and lungs

SD rats were anesthetized with 7% chloralhydrate, and 500 μL of C6-loaded NPs was administered *via* intranasal instillation. Rats were sacrificed after 30 min, and the lungs along with the bronchi were carefully resected, fixed with 4% paraformaldehyde, and dehydrated with 30% sucrose. The samples were washed thrice with PBS, added to a 24-well plate filled with optimum cutting temperature (OCT) compound, and frozen in a −40 °C refrigerator. The tissues were sectioned, stained with DAPI, and imaged on the confocal laser scanning microscope (CLSM, Zeiss LSM 800, Germany).

4.6.2. Retention of NPs in the lungs

Male ICR mice were anesthetized with 7% chloralhydrate, and 50 μL of DiR-loaded NPs was administered *via* intranasal instillation. Mice were sacrificed at the predetermined time *via* cervical dislocation. Their heart, liver, spleen, lung, and kidney were harvested and rinsed in PBS. Imaging was performed with *in vivo* imaging system (IVIS Lumina 3, PerkinElmer, Massachusetts, USA) and semi-quantitative analysis was performed.

4.7. Mucus penetration ability study

4.7.1. Collection of cystic fibrosis sputum

Sputum samples spontaneously expectorated by cystic fibrosis (CF) patients were collected at the Clinical Laboratory of West China Hospital. Six samples were acquired, placed on ice, and pooled to minimize patient-to-patient variation. The procedures conformed to ethical standards, and the sputum sample collection was performed under informed consent on a protocol approved by the Clinical Laboratory of West China Hospital.

4.7.2. Mucus diffusion

The 3D Transwell system (Corning Costar, NY, USA) was applied to investigate the ability of NPs to permeate across mucus. Briefly, 50 μL of sputum was added uniformly on the Transwell polycarbonate membrane (3 μm, 0.33 cm^2). After equilibration for 30 min, the donor chambers were added carefully with 200 μL of PBS containing C6-loaded NPs, and the acceptor chambers were added with 800 μL PBS. The samples were incubated at 37 °C. At predetermined time intervals, samples (80 μL) were removed from acceptor chambers and equal volumes of fresh PBS were supplemented. Finally, the sample solution was broken by DMSO, and the fluorescence intensity was detected by a microplate reader.

4.7.3. Multiple particle tracking

The *ex vivo* tracking of NPs was performed in human CF sputum. C6-loaded NPs were mixed with sputum and incubated for 30 min at 37 °C. The tracking of NPs was recorded using a nanoparticle tracking analysis (NTA, NanoSight LM10, UK). The particle averaged mean squared displacement (MSD) was calculated by the following equation:

$$MSD_\tau = [x_{(t+\tau)}\text{-}x_t]^2+[y_{(t+\tau)}\text{-}y_t]^2 \quad (1)$$

$$D_{eff} = \frac{MSD}{4\tau} \quad (2)$$

Where x and y represent the NPs coordinates at a given time scale (t) and τ indicates the time interval.

4.8. Endocytosis

4.8.1. Cellular uptake study

Before internalization studies, the cell density was estimated by Alamar Blue assay. Then the Calu-3 cells were incubated with C6-loaded NPs for 3 h and washed three times with fresh PBS. Finally, the cells were lysed by DMSO and the fluorescence intensity was measured by a microplate reader. For the qualitative study, the Calu-3 cells were incubated with C6-loaded NPs and stained with DAPI. A CLSM was used to observe and collect the images.

4.8.2. Binding avidity study

The cell density was estimated by Alamar Blue assay. Then the Calu-3 cells were pretreated at 4 °C for 30 min. Then, Calu-3 cells were incubated with C6-loaded NPs at 4 °C for 1 h. The fluorescence intensity was measured by a microplate reader.

4.8.3. Actin arrangement study

After incubating with lysophosphatidic acid (LPA, 3 μM) for 0.5 h, Calu-3 cells were incubated with C6-loaded NPs for 1 h. The

fluorescence intensity was measured by a microplate reader.

For actin filaments staining, Calu-3 cells were plated on coverslips and incubated at 37 °C for 3 days. C6-loaded NPs were added to the dishes and incubated at 37 °C for 1 h. The polymerized actin filaments were stained with rhodamine-phalloidin and the nucleus was stained with DAPI. The images were acquired by the CLSM.

4.9. Exocytosis

4.9.1. Intracellular trafficking study

For the co-localization study, Calu-3 cells were incubated with C6-loaded NPs for 2 h and then treated with trackers of subcellular organelles. ER-tracker Red and Golgi-tracker Red were used, according to the instructions. DAPI was used to stain the nucleus and the CLSM was used to visualize. The Pearson correlation coefficient Rr was calculated by Image-Pro Plus.

4.9.2. Exocytosis of NPs

The Calu-3 cells were cultured in 96-well plates incubated with C6-loaded NPs for 3 h. After washing three times with PBS, the cells were incubated with media for another 3 h. The fluorescence intensity in cells was measured.

4.9.3. Measurement of calcium

The Calu-3 cells were incubated with Fluo-4 AM (5 μM) at 37 °C for 30 min. NPs were added to the Fluo-4-loaded cells and then measured at 490 nm excitation and 520 nm emission every 10 s for 10 min.

For time-lapse imaging, Calu-3 cells were seeded into glass-bottom cell culture dishes and then cultured in 3 days. The cells were treated with Fluo-4 AM (5 μM) at 37 °C for 30 min. The dish was placed horizontally on the stage of CLSM, and a blank NPs solution was added into the dish carefully. The x-y-t program in CLSM was used to collect images every 10 s for 10 min.

4.9.4. Colocalization of early endosomes with endoplasmic reticulum

The colocalization of early endosomes with the endoplasmic reticulum (ER) was detected by immunofluorescence. The Calu-3 cells were incubated with C6-loaded NPs for internalization, the ER stained with ER-tracker blue, and the early endosomes labeled with Rab5. The rabbit anti-Rab5 was used as previously reported [47]. The images were observed *via* CLSM.

4.10. Statistical analysis

All data were presented as mean ± standard deviations (SD). Two-tailed Student's t-test and one-way analysis of variance (ANOVA) with Tukey's post-hoc test were used to test for statistical significance between groups. The differences were considered statistically significant for $p < 0.05$, $p < 0.01$, $p < 0.001$.

Data statement

The data that support the findings of this study are available from the corresponding author upon reasonable request.

Ethics approval and consent to participate

All animal experiments were approved by the Institutional Animal Care and Use Committee of Sichuan University (accreditation number, SYXK (Chuan) 2018-113).

CRediT authorship contribution statement

Yinglan Yu: Conceptualization, Investigation, Methodology, Formal analysis, Data curation, Writing – original draft. **Shujie Li:** Writing – review & editing. **Yuan Yao:** Data curation, Methodology. **Xinran Shen:** Data curation, Methodology. **Lian Li:** Writing – review & editing. **Yuan Huang:** Project administration, Supervision, Funding acquisition, Writing – review & editing.

Declaration of competing interest

The authors declare no competing financial interests.

Acknowledgments

The authors acknowledge financial support from the National Science Foundation for Distinguished Yong Scholars (81625023), the National Natural Science Foundation of China (81872818).

Appendix A. Supplementary data

Supplementary data to this article can be found online at https://doi.org/10.1016/j.bioactmat.2022.06.016.

References

[1] S. Azarmi, W.H. Roa, R. Löbenberg, Targeted delivery of nanoparticles for the treatment of lung diseases, Adv. Drug Deliv. Rev. 60 (8) (2008) 863–875.
[2] W. Yang, J.I. Peters, R.O. Williams, Inhaled nanoparticles-A current review, Int. J. Pharm. 356 (1–2) (2008) 239–247.
[3] J.S. Suk, S.K. Lai, N.J. Boylan, M.R. Dawson, M.P. Boyle, J. Hanes, Rapid transport of muco-inert nanoparticles in cystic fibrosis sputum treated with N-acetyl cysteine, Nanomedicine 6 (2) (2011) 365–375.
[4] J. Todoroff, R. Vanbever, Fate of nanomedicines in the lungs, Curr. Opin. Colloid Interface Sci. 16 (3) (2011) 246–254.
[5] K.P. O'Donnell, H.D. Smyth, Macro-and microstructure of the airways for drug delivery, in: Controlled Pulmonary Drug Delivery, Springer, 2011, pp. 1–19.
[6] S. Weber, A. Zimmer, J. Pardeike, Solid lipid nanoparticles (SLN) and nanostructured lipid carriers (NLC) for pulmonary application: a review of the state of the art, Eur. J. Pharm. Biopharm. 86 (1) (2014) 7–22.
[7] J.S. Patton, R.R. Byron, Inhaling medicines: delivering drugs to the body through the lungs, Nat. Rev. Drug Discov. 6 (1) (2007) 67–74.
[8] J. Panyam, V. Labhasetwar, Biodegradable nanoparticles for drug and gene delivery to cells and tissue, Adv. Drug Deliv. Rev. 55 (3) (2003) 329–347.
[9] E. Allémann, J.C. Leroux, R. Gurny, Polymeric nano- and microparticles for the oral delivery of peptides and peptidomimetics, Adv. Drug Deliv. Rev. 34 (2) (1998) 171–189.
[10] B.S. Schuster, A.J. Kim, J.C. Kays, M.M. Kanzawa, W.B. Guggino, M.P. Boyle, Overcoming the cystic fibrosis sputum barrier to leading Adeno-associated virus gene therapy vectors, Mol. Ther. 22 (8) (2014) 1484–1493.
[11] Q. Liu, J. Guan, L. Qin, X. Zhang, S. Mao, Physicochemical properties affecting the fate of nanoparticles in pulmonary drug delivery, Drug Discov. Today 25 (1) (2020) 150–159.
[12] S.H. van Rijt, T. Bein, S. Meiners, Medical nanoparticles for next-generation drug delivery to the lungs, Eur. Respir. J. 44 (2014) 765–774.
[13] A.M. Shen, T. Minko, Pharmacokinetics of inhaled nanotherapeutics for pulmonary delivery, J. Contr. Release 326 (10) (2020) 222–244.
[14] T.C. Carvalho, J.I. Peters, R.O. Williams, Influence of particle size on regional lung deposition-what evidence is there? Int. J. Pharm. 406 (1–2) (2011) 1–10.
[15] M. Smola, T. Vandamme, A. Sokolowski, Nanocarriers as pulmonary drug delivery systems to treat and to diagnose respiratory and non respiratory diseases, Int. J. Nanomed. 3 (1) (2008) 1–19.
[16] A.H. Chow, H.H. Tong, P. Chattopadhyay, B.Y. Shekunov, Particle engineering for pulmonary drug delivery, Pharm. Res. (N. Y.) 24 (3) (2007) 411–437.
[17] U.K. Marelli, F. Rechenmacher, T.R.A. Sobahi, C. Mas-Moruno, H. Kessler, Tumor targeting via integrin ligands, Front. Oncol. 3 (2013) 222.
[18] J. Sudimack, R.J. Lee, Targeted drug delivery via the folate receptor, Adv. Drug Deliv. Rev. 41 (2) (2000) 147–162.
[19] T.R. Daniels, E. Bernabeu, J.A. Rodríguez, S. Patel, M. Kozman, D.A. Chiappetta, The transferrin receptor and the targeted delivery of therapeutic agents against cancer, Biochim. Biophys. Acta 1820 (3) (2012) 291–317.
[20] J. Sun, L. Zhang, J. Wang, Q. Feng, D. Liu, Q. Yin, D. Xu, Y. Wei, B. Ding, X. Shi, X. Y. Jiang, Tunable rigidity of (polymeric core)-(lipid shell) nanoparticles for regulated cellular uptake, Adv. Mater. 27 (8) (2015) 1402–1407.
[21] Y. Yu, L. Xing, L. Li, J. Wu, J. He, Y. Huang, Coordination of rigidity modulation and targeting ligand modification on orally-delivered nanoparticles for the treatment of liver fibrosis, J. Contr. Release 341 (2021) 215–226.
[22] P.M. Valencia, O.C. Farokhzad, R. Karnik, R. Langer, Microfluidic technologies for accelerating the clinical translation of nanoparticles, Nat. Nanotechnol. 7 (10) (2012) 623–629.
[23] A.J. Bitonti, J.A. Dumont, S.C. Low, R.T. Peters, K.E. Kropp, V.J. Palombella, Pulmonary delivery of an erythropoietin Fc fusion protein in non-human primates through an immunoglobulin transport pathway, Proc. Natl. Acad. Sci. USA 101 (26) (2004) 9763–9768.

[24] G.M. Spiekermann, P.W. Finn, E.S. Ward, J. Dumont, B.L. Dickinson, R. S. Blumberg, Receptor-mediated immunoglobulin G transport across mucosal barriers in adult life: functional expression of FcRn in the mammalian lung, J. Exp. Med. 196 (3) (2002) 303–310.
[25] C.S. Schneider, Q. Xu, N.J. Boylan, J. Chisholm, B.C. Tang, B.S. Schuster, Nanoparticles that do not adhere to mucus provide uniform and long-lasting drug delivery to airways following inhalation, Sci. Adv. 3 (4) (2017), e1601556.
[26] H. Derendorf, Pharmacokinetic and pharmacodynamic properties of inhaled corticosteroids in relation to efficacy and safety, Respir. Med. 91 (1) (1997) 22–28.
[27] D. Mehta, A.B. Malik, Signaling mechanisms regulating endothelial permeability, Physiol. Rev. 86 (1) (2006) 279–367.
[28] M.A. Matthay, G.A. Zimmerman, Acute lung injury and the acute respiratory distress syndrome: four decades of inquiry into pathogenesis and rational management, Am. J. Respir. Cell Mol. Biol. 33 (2005) 319–327.
[29] E. Lundeberg, D. Van, E. Kenne, O. Soehnlein, L. Lindbom, Assessing large-vessel endothelial permeability using near-infrared fluorescence imaging-brief report, Arterioscler. Thromb. Vasc. Biol. 35 (2015) 783–786.
[30] M. Kaya, B. Ahishali, Assessment of permeability in barrier type of endothelium in brain using tracers: evans blue, sodium fluorescein, and horseradish peroxidase, Methods Mol. Biol. 763 (2011) 369–382.
[31] M. Ehrlich, W. Boll, A.V. Oijen, R. Hariharan, T. Kirchhausen, Endocytosis by random initiation and stabilization of clathrin-coated pits, Cell 118 (5) (2004) 591–605.
[32] Z. Kadlecova, S.J. Spielman, D. Loerke, A. Mohanakrishnan, D.K. Reed, S.L. Schmid, Regulation of clathrin-mediated endocytosis by hierarchical allosteric activation of AP2, J. Cell Biol. 216 (1) 2017 167-179.
[33] D. Devadas, T. Koithan, R. Diestel, U. Prank, B. Sodeik, K. Döhner, Herpes simplex virus internalization into epithelial cells requires Na+/H+ exchangers and p21-activated kinases but neither clathrin- nor caveolin-mediated endocytosis, J. Virol. 88 (22) 2014 13378-13395.
[34] M. Koivusalo, C. Welch, H. Hayashi, C.C. Scott, M. Kim, T. Alexander, N. Touret, K. M. Hahn, S. Grinstein, Amiloride inhibits macropinocytosis by lowering submembranous pH and preventing Rac1 and Cdc42 signaling, J. Cell Biol. 188 (2010) 547–563.
[35] Y. Yu, Z. Wu, J. Wu, X. Shen, R. Wu, M. Zhou, L. Li, Y. Huang, Investigation of FcRn-mediated transepithelial mechanisms for oral nanoparticle delivery systems, Adv. Ther. (2021) 1–13, 2100145.
[36] K.A. Beningo, Y.L. Wang, Fc-receptor-mediated phagocytosis is regulated by mechanical properties of the target, J. Cell Sci. 115 (4) (2002) 849–856.
[37] J.S. Koh, W. Lieberthal, S. Heydrick, J.S. Levine, Lysophosphatidic acid is a major serum noncytokine survival factor for murine macrophages which acts via the phosphatidylinositol 3-kinase signaling pathway, J. Clin. Invest. 102 (4) (1998) 716–727.
[38] R.C. May, L.M. Machesky, Phagocytosis and the actin cytoskeleton, J. Cell Sci. 114 (6) (2001) 1061–1077.
[39] P.D. Knecht, The regulation of actin polymerization and cross-linking in Dictyostelium, Biochim. Biophys. Acta 1525 (3) (2001) 217–227.
[40] H. Aizawa, Y. Fukui, I. Yahara, Live dynamics of Dictyostelium cofilin suggests a role in remodeling actin latticework into bundles, J. Cell Sci. 110 (19) (1997) 2333–2344.
[41] E. Lee, E.A. Shelden, D.A. Knecht, Changes in actin filament organization during pseudopod formation, Exp. Cell Res. 235 (1) (1997) 295–299.
[42] J.J. Rudd, V.E. Franklin-Tong, Calcium signaling, Cell 80 (2) (1995) 259–268.
[43] J.W. Putney, Store-operated Calcium Channels, Handbook of Cell Signaling, vol. 113, Elsevier Inc., 2010, pp. 911–914.
[44] E. Gagnon, J.J. Bergeron, M. Desjardins, ER-mediated phagocytosis: myth or reality? J. Leukoc. Biol. 77 (6) (2005) 843–845.
[45] D. Michel, ER-mediated phagocytosis: a new membrane for new functions, Nat. Rev. Immunol. 3 (4) (2003) 280–291.
[46] R. Luo, L. Tang, S. Zhong, Z. Yang, J. Wang, Y. Weng, In vitro investigation of enhanced hemocompatibility and endothelial cell proliferation associated with quinone-rich polydopamine coating, ACS Appl. Mater. Interfaces 5 (2013) 1704–1714.
[47] Y.X. Zheng, L.Y. Xing, L. Chen, R. Zhou, J.W. Wu, X. Zhu, L. Li, Y.C. Xiang, R. N. Wu, L. Zhang, Y. Huang, Tailored elasticity combined with biomimetic surface promotes nanoparticle transcytosis to overcome mucosal epithelial barrier, Biomaterials 262 (2020), 120323.